Chapter 6

Magnetotelluric reconnaissance of the Nisyros Caldera and Geothermal Resource (Greece)

Andreas Tzanis[1], Vassilis Sakkas[2] and Evangelos Lagios

Section of of Geophysics and Geothermy,
Department of Geology and the Geoenvironment,
National and Kapodistrian University of Athens,
Panepistimiopoli, Zografou 15784, Greece;
[1] atzanis@geol.uoa.gr; [2] vsakkas@geol.uoa.gr; [3] lagios@geol.uoa.gr

Appears in:

Dietrich, V.J. and Lagios, E. (eds),
"Nisyros Volcano: The Kos - Yali - Nisyros Volcanic Field",
Springer Verlag, pp. 203-225, 2017.
DOI: 10.1007/978-3-319-55460-0.

Athens, August 2017

Abstract

A Magnetotelluric reconnaissance survey of 39 soundings was carried out in the caldera of Nisyros, a small island volcano at the eastern end of the Hellenic Volcanic Arc (HVA), Greece, in an attempt to explore the high temperature geothermal resource of the area. Iteratively reweighted least squares was implemented to compute stable and smooth Earth response functions exhibiting 2-D to weakly 3-D attributes, as a result of induction in low-contrast local geoelectric inhomogeneities, superimposed on a dominantly 2-D background structure; coastal and island induction effects are absent due to the low offshore/onshore resistivity contrast at, and below sea level. Application of advanced hypothetical event analysis techniques to study the spatial properties of the telluric field demonstrated that convection and hydrothermal circulation is controlled by a system of antithetic NE-SW oriented active normal faults which form a graben-like structure and define the 2-D background, as well as a conjugate system of NNW-SSE normal faults which is particularly active at the SW quadrant of the island and define the main convection path. It was determined that under these conditions the data could be interpreted with 2-D inversion, which has successfully reconstructed detailed images of the structural and functional elements of the hydrothermal system. The structural elements include a number of shallow hot water reservoirs in the argillic and phyllic alteration zones and a laterally extended deep (approx. 1km) circulation zone, all embedded in a low-resistivity with very low lateral contrasts. The functional elements include images of the most important convection conduits created by the intersection of major fault planes. The results are corroborated by the logs of two deep exploration wells. Overall, on the basis of a carefully reworked data set, our analysis has provided detailed images of the volcano's interior and valuable insight into its structure, function and geothermal potential.

1. Introduction

Nisyros is a small Quaternary island volcano, located at the eastern terminus of the Hellenic Volcanic Arc (36°35.25′N, 27°10.0′E, also see inset in Fig. 6.1). It is an active spot with a history of explosive eruptions, the largest of which formed a caldera dominating the landscape of the island. Immediately afterwards, extrusive activity covered the largest part of the caldera with rhyolitic domes, leaving in its eastern half a small elongate basin of NNE-SSW orientation (Lakki depression, see Fig. 6.1).

Lakki is defined by a system of NNE-SSW oriented antithetic normal faults forming a graben-like structure that contains a hydrothermal field and high temperature geothermal resource. For this reason, it has been subject to systematic exploration (Ungemach, 1983; Geotermica Italiana, 1983). Geophysical studies of the geothermal resource have been were conducted between 1989 and 1992 by carrying out Magnetotelluric (MT) surveys both in Lakki and at the southern extension the Lakki graben, with funding from the Public Power Corporation (PPC) of Greece, Department of Alternative Energy Resources. Some results of these investigations have already been reported by Lagios, (1991), Dawes and Lagios, (1991) and Lagios et al., (1991). The MT surveys were followed by a multi-parametric study of the southern extension of the Lakki graben comprising self-potential, gravity and VLF measurements (Lagios and Apostolopoulos, 1995). The geophysical surveys were conducted under an outstanding requirement of highly accurate results within the first 2km, including the detection and delineation of reservoir structures with a high degree of confidence and, if possible, the successful detection of geothermal fluid convection and circulation conduits for subsequent evaluation of energy resources.

The previous geophysical work has basically been successful but the analysis and interpretation of the data was based on methods and techniques of that time (1989–1995). The present paper is devoted to a qualitative and quantitative re-examination of the Magnetotelluric data using improved data processing methods, new hypothetical event analysis techniques to study the spatial configuration of the telluric field and two-dimensional inversion tools. It will be shown that the results vastly expand previous knowledge of the interior structure of the geothermal resource. The results also demonstrate the capability of the Magnetotelluric method to image and delineate fine structural details when accurate data is available; high resolution images of a small albeit complex geothermal system including convection paths, reservoirs and reservoir related structures are adequately reconstructed and discussed.

2. The Nisyros Volcanic Complex and Geothermal Resource

The South Kos and Nisyros volcanic field has been active for at least 3Ma and continues to show signs of contemporary unrest (e.g. Papadopoulos et al, 1998; Sachpazi et al, 2002; Lagios et al, 2005). Accordingly, it has been the focus of significant research effort which has produced a general model of the petrological, volcanological and tectonic evolution of the area (Davis, 1967; Di Paola, 1974; Keller, 1982; Ungemach, 1983; Geotermical Italiana, 1983; Bohla and Keller, 1987; Vougioukalakis, 1989, 1993; Seymour and Vlassopoulos, 1989, 1992; Wyers and Barton, 1989; Papanikolaou et al., 1991; Limburg and Varekamp, 1991; Varekamp, 1992; Francalanci et al, 1995; Papanikolaou and Nomikou, 2001; Volentik et al., 2006; Vanderkluysen et al., 2006a, 2006b; Bachman et al., 2011; Nomikou and Papanikolaou, 2011).

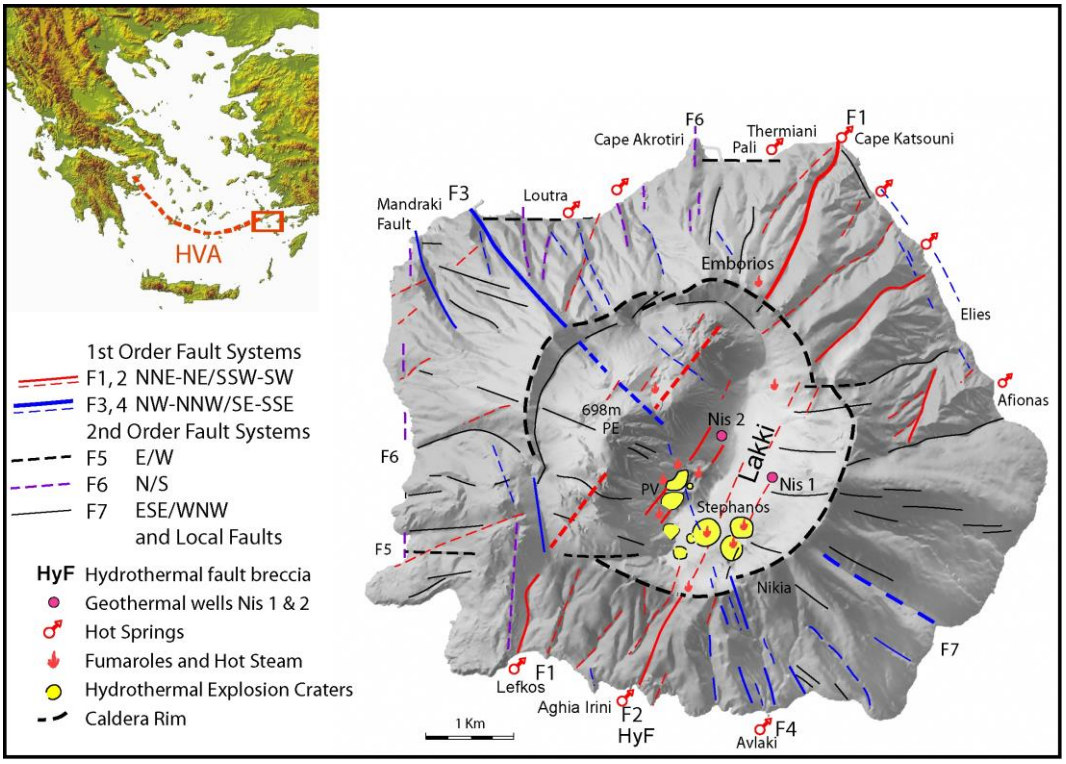

Figure 6.1: Shaded relief image of Nisyros Island, (36°35.25′N, 27°10.0′E), including the major fault zones, hydrothermal activity sites and important toponyms; the image was modified from Lagios et al., (2005). The inset map at the top-left indicates the location of Nisyros (red rectangle) in the Hellenic (South Aegean) Volcanic Arc (red dashed line). PE stands for Prophetes Elias; PV for the Polyvotis phreatic explosion crater. The figure was modified Lagios et al., (2005).

Focusing on Nisyros, it is generally accepted that its geological evolution comprises four stages. The pre-caldera stage, (300-30Ka BCE), builds the volcanic edifice with extrusive activity through a basement consisting of Mesozoic limestone and Neogene sediments, in several successive phases from underwater andesitic to subaerial dacitic and rhyo-dacitic. K-Ar and δC^{14} dating, as well as tephrostratigraphy and the absence of the Kos Plateau Tuff deposits (of about 161 Ka BCE) suggest that the subaerial part of Nisyros formed during the last 161 Ka (Francalanci et al, 2005); during this stage significant tectonic activity creates the fault zones F1, F2 and F3. The caldera formation stage follows between 44 – 24Ka BCE and comprises two or three phases, each commencing with low-intensity phreatomagmatic explosions fed by rhyolitic magmas; these destroy the volcanic edifice by ejecting a few km^3 of debris and triggering a central caldera collapse. The post-caldera stage begins with extrusion of the rhyolitic – dacitic Prophetes Elias domes and lava flows, which cover the western part of the caldera only (approx. 24Ka BCE). The major fault zones continue being active. During the contemporary stage volcanic activity died out. The major fault zones have reactivate and the (youngest) F4 zone is incited. Secondary faulting episodes take place as well. Intense and often violent hydrothermal activity also occurs with several episodes of phreatic explosions in historic times (1422 – 1888 CE). The signatures of at least 11 phreatic explosions are apparent; the greatest of them has formed the Stephanos Crater, an impressive depression of 20-30m with a longest dimension of 300m.

The major fault zones shown in Fig. 6.1 are important in the historic geotectonic and morphological evolution of the volcano and, simultaneously, control contemporary convection and hydrothermal

activity. Every single phreatic explosion took place at, or near the intersections of the major fault zones. Accordingly, we it is helpful to provide a brief description:

- The normal fault zone **F1** is striking at N30°, dipping at 70°-80° to the NE with a throw of approx. 100m. It can clearly be seen within the caldera, comprising a series of large parallel faults producing obvious morphological discontinuities on the eastern flank of the Prophetes Elias domes. Appreciable hydrothermal activity, with fumaroles and intense alterations can be seen along its strike. The F1 system appears to have been important for the placement of the post-caldera dacites, whose eruptive centers are aligned in a N30°-40° direction; inasmuch as the magmas feeding these extrusions originated in deep crustal chambers, it seems that F1 comprises a deep reaching zone of crustal weakness.
- The normal fault zone F2 is also striking at N30° and dipping at 70°-80° to the WNW, with a throw of 100 – 120m. It forms a tectonic graben with the oppositely dipping F1 and while it produces impressive escarpments outside the caldera its presence within is obscure although it is thought to cross the Stephanos phreatic explosion crater. At the coast of Aghia Irini, southwest of Lakki, F2 is associated with underwater thermal springs with temperatures 40-50°C.
- The normal fault zone **F3** appears at the NW part of the island with a strike of N320°-330°, dip 70°-80° to the NE and throw of more than 100m. It has been verified outside the caldera near the town of Mandraki. Its trace is uncertain in the area of the Prophetes Elias domes, except for a large elongate morphological feature along its projected continuation, where it is thought to separate the main outcrops of the Prophetes Elias lava domes from the smaller domes to the northeast. F3 appears again as a morphological discontinuity on the NW flank of Lakki, while branches of the system are thought to extend through the Polyvotis and Micros Polyvotis phreatic explosion craters into Stephanos and further SE to the Avlaki and Aghia Irini areas.
- The fault zone **F4** appears to play an important role in the formation and functioning of the geothermal field. It forms a graben like depression with two principal and a series of secondary faults, striking N340° and dipping at 70°-80°. Its presence is obvious, inasmuch as it produces dislocation of the caldera rim. Contemporary fumarolic activity and at least 11 phreatic explosion features are located at the intersections of F4 with the system F1/F2. In addition, the debris flow and lacustrine deposits related to the 1873 CE hydrothermal explosion events exhibit a clear N340° distribution, collocated with the trace of the F4 system (shaded area in Fig. 6.5). At the Avlaki area, at the SE end of the island, F4 is associated with underwater thermal springs with temperatures of 60°C.

Additional to the major faults, three secondary faulting structures can be identified; these are labelled F5, F6 and F7 in Fig. 6.1; albeit minor, they can still influence the circulation and diffusion of hydrothermal fluids with particular reference to F5 and F7. The F5 and F7 systems are oriented E-W and ESE-WNW respectively. They both may result from the interaction between the F1 and F3. Members of this system which will be shown to have a notable effect on the resistivity structure are expressed in the area between Lakki, Elies and Afionas. The thermal spring of Afionas at sea level might also be a result of these faults.

These fault zones produce a number of neotectonic blocks, each characterized by its relative uplift, as determined by differential InSAR and GPS observations (Lagios et al, 2005). Maximum uplift and westward to SW-ward horizontal displacement is observed at the western (Prof. Elias) block, which incorporates the Mount of Prophetes Elias and surrounding summits and is bounded by the F1 and F3

fault zones. Minimum uplift and SE-ward displacement is observed at the Lakki - Aghia Irini graben, bounded by F1, F2 and F4. Intermediate uplift and eastward displacement is observed at the eastern (Nikia) block, bounded by F4, F2 and F5/F7, and at the northern (Emporio) block, bounded by F5/F7, F2 and F3. It is therefore clear that the major and secondary normal fault zones impart divergent differential motion between the west, south and east sectors of the island, thus facilitating the convection and circulation of hydrothermal fluids.

3. The Magnetotelluric Survey

3.1 Acquisition and Processing

The Magnetotelluric data was collected with funding from the Public Power Corporation of Greece, Department of Alternative Energy Resources and in cooperation with the Department of Geology and Geophysics of the University of Edinburgh (Mr G.J.K. Dawes). The survey was conducted in two phases and comprised a total of 39 soundings, the locations of which are shown in Fig. 6.2. Phase I was carried out in June 1989 and comprised 20 soundings at the southern and central part of Lakki, indicated by code numbers '9xx' in Fig. 6.2; Phase II was carried out in May 1991 and comprised 19 soundings indicated by the code numbers '1xx'. A 1-D interpretation of the Phase I data has already been reported by Dawes

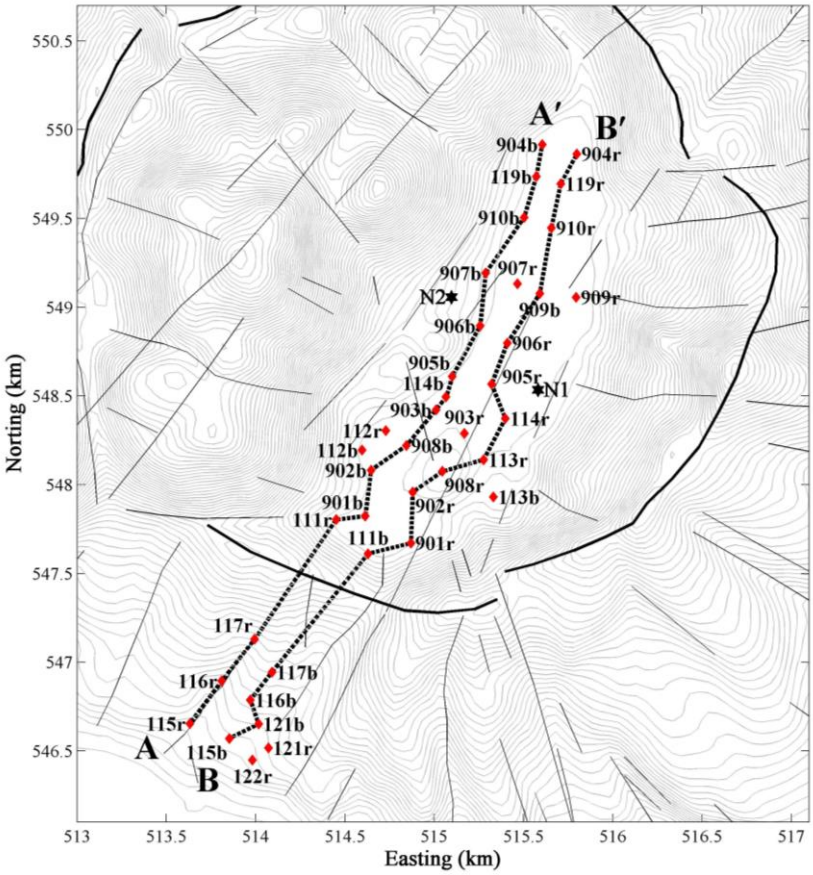

Figure 6.2: Location of the 39 magnetotelluric sounding sites. N1 and N2 are the positions of the two deep exploration wells. The dashed lines AA′ and BB′ indicate the Transects along which 2-D inversion has been carried out.

and Lagios (1991).

The measurements were carried out with the Short Period Automatic Magnetotelluric system (SPAM) MkIIb, developed by Dawes (1984), in the nominal frequency bandwidth 128Hz-40s, using $Pb/PbCl_2$ electrodes and CM11 induction coils. The Magnetotelluric – Telluric measurement mode was implemented, using a 5-component Magnetotelluric configuration at the *Base* site and a 2-component Telluric configuration at a single *Remote* (satellite) site. The Telluric – Magnetotelluric method requires uniformity of the source field over the base and satellite stations, an assumption valid if they are separated by relatively short distances. At the base station (indicated by B) one measures the horizontal transverse components of the MT field $\mathbf{E}_B=[E_{xB}\ E_{yB}]^{\mathrm{T}}$ and $\mathbf{H}_B=[H_{xB}\ H_{yB}]^{\mathrm{T}}$, whence the impedance tensor $\mathbf{Z}_B$ can be computed. At the satellite stations (indicated by R), only the telluric field components are measured, i.e. $\mathbf{E}_R=[E_{xR}\ \ E_{yR}]^{\mathrm{T}}$. Then,

$$\mathbf{E}_R = \mathbf{T}\cdot\mathbf{E}_{\boldsymbol{B}} \Leftrightarrow \mathbf{E}_R = \mathbf{T}\cdot\mathbf{Z}_B\cdot\mathbf{H}_B \Leftrightarrow \mathbf{E}_R = \mathbf{Z}_M\cdot\mathbf{H}_B$$

where $\mathbf{T}$ is the *telluric transfer tensor* defined as

$$\begin{pmatrix} E_{xR} \\ E_{yR} \end{pmatrix} = \begin{pmatrix} T_{xx} & T_{xy} \\ T_{yx} & T_{yy} \end{pmatrix} \cdot \begin{pmatrix} E_{xB} \\ E_{yB} \end{pmatrix}$$

and $\mathbf{Z}_{\boldsymbol{M}}$ is the *impedance transfer tensor* by which the base magnetic field $\mathbf{H}_{\boldsymbol{B}}$ is referred to the remote telluric field $\mathbf{E}_{\boldsymbol{R}}$.

Given that remote referencing was unavailable at the time of data collection, the Earth responses were estimated in two stages. The first stage comprised standard single-site processing techniques: on the assumption of stochastic (Gaussian) time processes the impedance tensor elements were computed with the least squares solution of the two-input one-output linear system

$$E_i = Z_{ix}H_x + Z_{iy}H_y + \varepsilon_i, \qquad i = x, y,$$

by minimising the noise ε_i (Sims et al., 1971). The quality of the solution can be monitored by means of the predicted coherence function

$$\gamma^2_{1.23} = \hat{E}_i / E_i = \hat{Z}_{ix}H_x + \hat{Z}_{iy}H_y, \qquad i = x, y,$$

where $\hat{E}_i$ represents the output electric field component predicted from the estimated elements $\hat{Z}_{ij}$. The estimation of Earth response functions was improved using a robust procedure quite similar to that of Egbert and Booker (1986). The spectral components E_x, E_y, H_x and H_y that yielded impedance tensor realizations with predicted coherence above 0.8 were cast into a system of the form

$$\begin{pmatrix} \Re(E_{i_1}) \\ \Im(E_{i_1}) \\ \Re(E_{i2}) \\ \Im(E_{i_2}) \\ \cdots \\ \Re(E_{i_N}) \\ \Im(E_{i_N}) \end{pmatrix} = \begin{pmatrix} \Re(H_{x_1}) & -\Im(H_{x_1}) & \Re(H_{y_1}) & -\Im(H_{y_1}) \\ \Im(H_{x_1}) & \Re(H_{x_1}) & \Im(H_{y_1}) & \Re(H_{y_1}) \\ \Re(H_{x_2}) & -\Im(H_{x_2}) & \Re(H_{y2}) & -\Im(H_{y_2}) \\ \Im(H_{x_2}) & \Re(H_{x_2}) & \Im(H_{y_2}) & \Re(H_{y_2}) \\ \cdots & \cdots & \cdots & \cdots \\ \Re(H_{x_N}) & -\Im(H_{x_N}) & \Re(H_{y_N}) & -\Im(H_{y_N}) \\ \Im(H_{x_N}) & \Re(H_{x_N}) & \Im(H_{y_N}) & \Re(H_{y_N}) \end{pmatrix} \cdot \begin{pmatrix} \Re(Z_{ix}) \\ \Im(Z_{ix}) \\ \Re(Z_{iy}) \\ \Im(Z_{iy}) \end{pmatrix}, \qquad i = x, y,$$

which was subsequently solved with iteratively reweighted least squares using MATLAB's™ robust multi-linear regression tool (for a formal description of the method see Huber, 1981). This algorithm may effectively downweight the influence of non-Gaussian noise, provided that the population of noise-free

data dominates the population of noisy data. Its performance is a function of noise and data statistics, progressively deteriorating as the probability of receiving noise waveforms increases, until breakdown when the noise is as likely as the data and can cloak the distribution of the noise-free population beyond recognition and recovery. In this event, the treatment must be case-specific. Moreover, single-site robust methods cannot cope with continuous harmonic multiple-coherent noise, for obvious reasons. In such cases, noisy estimators of the impedance tensor elements were removed with a "low-tech" method, namely "expert judgment" and manual deletion. A similar processing procedure was used to estimate magnetic transfer functions, hence induction vectors. Typical examples of estimated (observed) Earth responses are shown in Fig. 6.3 and Fig. 6.4 (see below for details).

3.2 Spatial analysis and determination of geoelectric strike

The *spatial analysis* of the magnetotelluric Earth response endeavours to extract information about the configuration of the induced natural EM fields, which, in turn, depend on the geometry and configuration of lateral inhomogeneities in the geoelectric structure. Herein we implement an anti-symmetric reformulation of the *equivalent* Canonical and Singular Value Decompositions of Yee and Paulson, (1987) and LaToracca et al, (1986) respectively. These decompositions are *symmetric* and apply when the electric and magnetic fields are measured in different orthogonal coordinate frames associated by a rotation of 90°. Tzanis (2014) has shown that they constitute proper rotations in 3-D space based on the topology of the SU(2) rotation group and result in a characteristic state – characteristic value (generalized eigenstate – eigenvalue) formulation of the Magnetotelluric induction problem; he has also shown that they can be reformulated into an anti-symmetric decomposition, which is suitable for the analysis of *practical* Magnetotelluric measurements in which the electric and magnetic fields are referred to the *same* coordinate frame and is consistent with the conventional rotation applied in typical Magnetotelluric analysis. The anti-symmetric decomposition reduces the impedance tensor to the form

$$\mathbf{Z} = \boldsymbol{\mathcal{E}}(\theta_E, \Phi_E) \cdot \begin{bmatrix} 0 & \zeta_1 \\ -\zeta_2 & 0 \end{bmatrix} \cdot \boldsymbol{\mathcal{H}}^{\dagger}(\theta_H, \Phi_H)$$

where (†) denotes Hermitian transposition and $\boldsymbol{\mathcal{E}}$ and $\boldsymbol{\mathcal{H}}$ are SU(2) rotation matrices, of the form

$$\boldsymbol{\mathcal{U}}(\theta, \Phi) = \begin{bmatrix} \cos\theta\cos\Phi - i\sin\theta\sin\Phi & -\cos\theta\sin\Phi + i\sin\theta\cos\Phi \\ \cos\theta\sin\Phi + i\sin\theta\cos\Phi & \cos\theta\cos\Phi + i\sin\theta\sin\Phi \end{bmatrix}$$

At any location on the surface of the Earth, the impedance tensor can be re-written as

$$\boldsymbol{\mathcal{E}}^{\dagger}\mathbf{Z} = \zeta \cdot \boldsymbol{\mathcal{H}}^{\dagger} \Rightarrow \begin{bmatrix} E_1(\theta_E, \Phi_E) \\ E_2(\theta_E, \Phi_E + \frac{\pi}{2}) \end{bmatrix} = \begin{bmatrix} 0 & \zeta_1 \\ -\zeta_2 & 0 \end{bmatrix} \cdot \begin{bmatrix} H_1(\theta_H, \Phi_H) \\ H_2(\theta_H, \Phi_H + \frac{\pi}{2}) \end{bmatrix}$$

with $\{E_1(\theta_E, \Phi_E), H_1(\theta_H, \Phi_H)\}$ comprising the *maximum* and $\{E_2(\theta_E, \Phi_E+\pi/2), H_2(\theta_H, \Phi_H+\pi/2)\}$ the *minimum characteristic states* (*eigenstates)* of the electromagnetic field.

The angles (θ_E, φ_E) define a *characteristic* coordinate frame or *eigen-frame* $\{x_E, y_E, z_E\}$ of the electric field, such that x_E is rotated by φ_E clockwise with respect to the x-axis of the experimental coordinate frame and the plane $\{x_E, y_E\}$ is tilted by an angle θ_E clockwise with respect to the horizontal plane $\{x, y\}$. Likewise, the angles (θ_H, φ_H) define the characteristic eigen-frame $\{x_H, y_H, z_H\}$ of the magnetic field such that x_H is rotated by φ_H clockwise with respect to the x-axis of the experimental coordinate frame and the

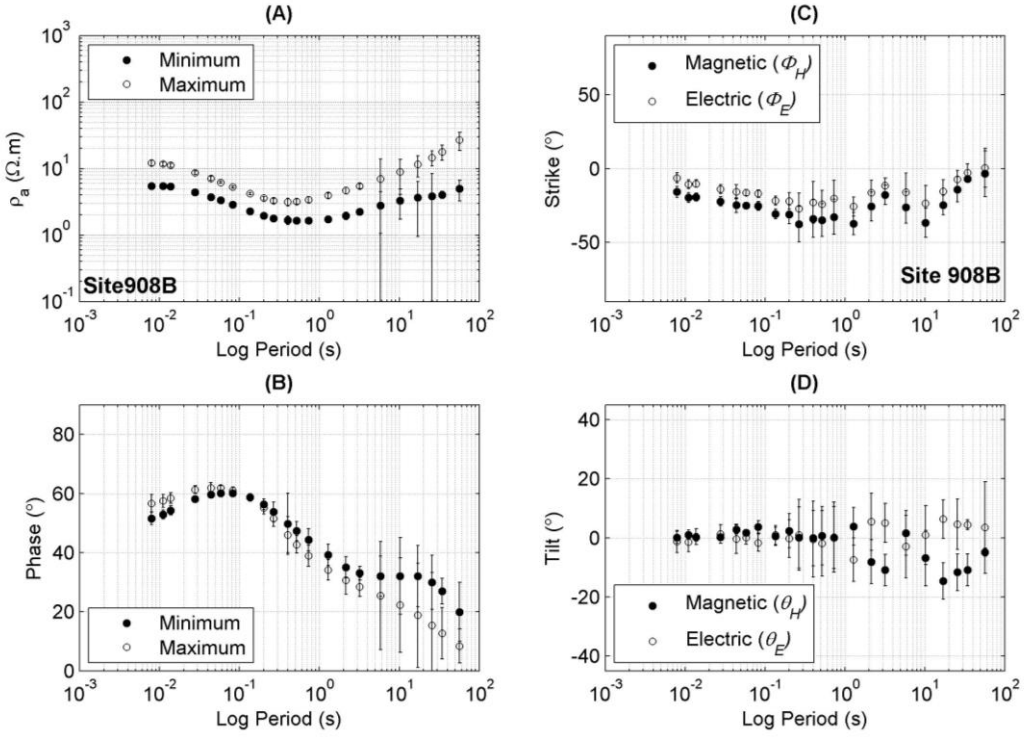

Figure 6.3: The maximum and minimum states of the impedance tensor at site 908B: (A) Maximum and minimum apparent resistivity; (B) maximum and minimum phase; (C) Strike of the Electric (Φ_E) and Magnetic (Φ_H) fields; (D) Tilt of the electric (θ_E) and magnetic (θ_H) fields.

plane $\{x_H, y_H\}$ is tilted by an angle θ_H clockwise with respect to the horizontal plane $\{x, y\}$. Each eigen-frame contains orthogonal, *linearly polarized* components. In the case of 2-D geoelectric structures, $\Phi_E = \Phi_H$ and $\theta_E = \theta_H = 0$. In 3-D structures however, it is possible that $\Phi_E \neq \Phi_H$ and/or $\theta_E \neq \theta_H \neq 0$. It follows that in each characteristic state, the associated electric and magnetic eigen-fields are not mutually perpendicular. It is equally important that the electric and magnetic eigen-frames are not horizontal. This should be of no surprise because in 3-D Earth structures the total magnetic and induced electric fields are three dimensional and may be associated with significant gradients, especially in the vicinity of interfaces. Accordingly, they are locally orthogonal and anti-symmetric in complex 3-space and the tilt angles θ_E and θ_H of the electric and magnetic eigen-frames are a measure of the local landscape of the electric and magnetic field respectively.

As a final point, it is important to note that the *projection* of the eigenstates on the *horizontal plane* comprise elliptically polarized components: the normalized projected field vector will have a major axis equal to $\cos\theta$ and a minor axis equal to $\sin\theta$. The ratio of the minor to the major axis is the *ellipticity*, given by $b = \tan\theta$ while $\theta > 0$ implies a counter-clockwise sense of rotation and $\theta < 0$ a clockwise sense. Thus, ellipticity on the horizontal plane is defined in terms of a rotation in higher dimensional space. It is not straightforward to see in this thrifty presentation, but the essence of this analysis is that it approaches the geoelectric structure as the equivalent of a birefringent material at low frequencies and large scales.

Fig. 6.3 illustrates the response of sounding 908B in the form of rotated impedance tensors. The data exhibit weak 3-dimensionality at short periods, evident in the variation of the maximum and minimum apparent resistivities and phases (Fig. 6.3a, b), as well as in the non-orthogonal configuration of the electric and magnetic eigen-frames for $T < 1$s (Fig. 6.3c). Moderate 3-dimensionality appears to develop

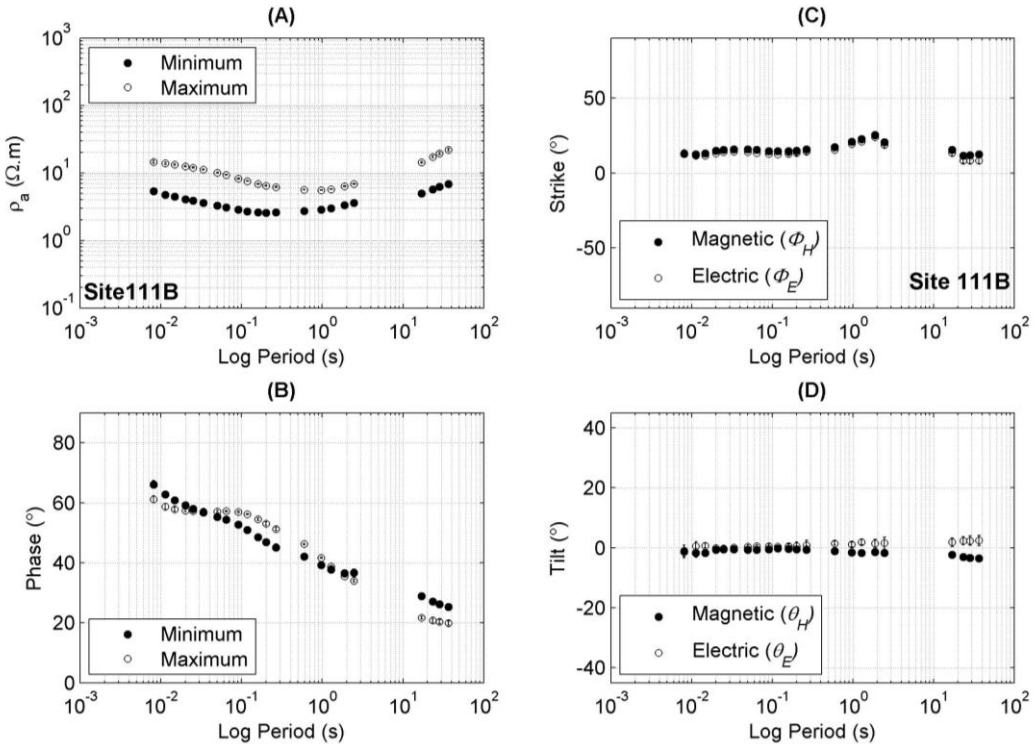

Figure 6.4: The maximum and minimum states of the impedance tensor at site 111B: (A) Maximum and minimum apparent resistivity; (B) maximum and minimum phase; (C) Strike of the Electric (Φ_E) and Magnetic (Φ_H) fields; (D) Tilt of the electric (θ_E) and magnetic (θ_H) fields.

at longer periods, as manifested by the variability of the strike angles Φ_E and Φ_H at $T > 0.3$s (Fig. 6.3c) and the non-trivial tilt of the electric and magnetic eigen-frames at periods longer than approx. 1s (Fig. 6.3d). Fig. 6.4 illustrates the Earth responses for sounding 111B as per Fig. 6.3. In this case, 2-D characteristics are evident in all the parameters of the maximum and minimum eigenstates, with the electric and magnetic field strikes being almost identical and the respective tilts generally trivial up to $T \approx$ 1s, with weak 3-D structural attributes appearing at periods longer than 10s.

The study of individual Earth responses indicates that the geoelectric structure is overall very conductive and generally 2-D or weakly 3-D at short periods, developing to weakly or moderately 3-D at long periods; it also appears to be complex, exhibiting significant lateral variation of the geoelectric strike and that the higher-dimensional inductive effects are generated by low-contrast local inhomogeneities. This general observation is confirmed by mapping the polarization ellipse of the maximum electric field and the real induction vector (RIV). Fig. 6.5 illustrates the configuration of these quantities, averaged over the period interval 2s – 100s (0.5Hz – 0.01Hz), which contains responses from the deeper and broader elements of the geoelectric structure.

Focusing on the spatial properties of the maximum electric field, we observe significant lateral variations in the principal direction of the geoelectric structure and may identify three domains with different apparent geoelectric strikes:

a) Outside of the caldera, at the SW of the Lakki graben, as well as inside the caldera and along the east side of Lakki, between sites 908R (Stephanos crater) and 119R, the orientation of the polarization ellipse is generally NNE-SSW and is consistent with the strike of the major F1, F2 fault zones and the trend of the Lakki graben.

b) Inside of the caldera, along the west flank of Lakki and between sites 902B and 905B, the orientation is generally NNW-SSE. This domain includes sites 902R and 901R and generally coincides with the trace of F4 fault zone.

c) Inside of the caldera, at the SW corner of the Lakki graben, as well as along its west flank between sites 906B and 119B, the orientation of the polarization ellipse is on average E-W and generally associated with the local strike of the depression.

Turning our attention to the real induction vectors, which are drawn in the Parkinson convention, we observe that inside the caldera, the RIV defines two domains with different apparent geoelectric strikes:

a) At the northern half of the Lakki depression, (north of site 906B), a NNE-SSW geoelectric trend is evident, consistent with the strike of F1 and F2 faults and the trend of the depression.

b) At the southern half of Lakki (south of sites 905B), a NNW-SSE geoelectric trend is clearly seen, consistent with the strike of the F4 fault zone.

The joint consideration of the maximum electric field and real IV configurations points toward the existence of a broader system of elongate background structures consistent with the 2-D approximation and associated with the F1/F2 faulting system, and a superimposed system of local elongate structures also fitting the 2-D approximation and collocated with the F4 faulting system. It also appears that the

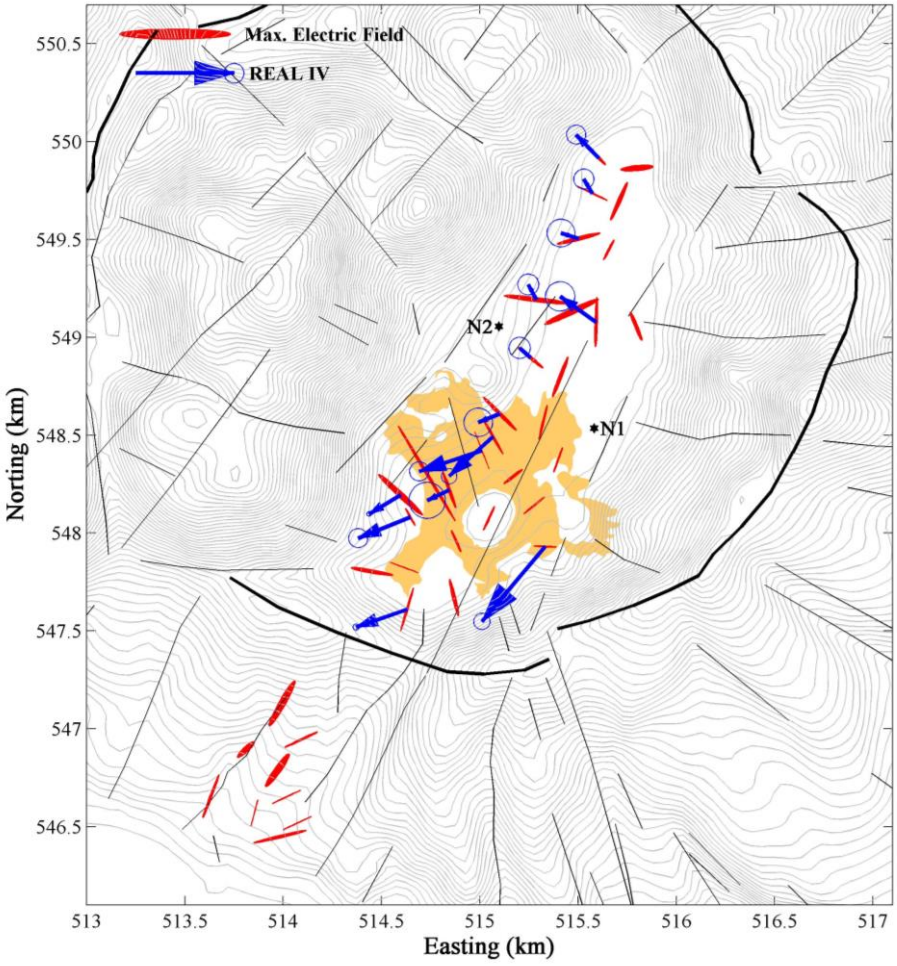

Figure 6.5: Configuration of the polarization state of the maximum electric field (red ellipses) and the real induction vectors (blue arrows); both are shown as averages over the bandwidth 2 – 100s. The shaded area indicates the extent of debris flow and lacustrine deposits related to the 1873 CE phreatic explosion events.

latter (F4) is associated with higher electrical conductivity and controls local induction and the flow of electric current. This would not only imply that the surface hydrothermal activity developing at the southern part of Lakki is associated with the intersections of F1, F2 and F4, but would also indicate that F4 is the main conduit for the ascent of geothermal fluids to the surface. Finally, local three-dimensionality is plainly evident in the spatial variability of the polarization ellipses and their non-orthogonal configuration with reference to the induction vectors.

The existence and strike of a broader, two-dimensional background geoelectric structure can also be investigated on the basis of the collective phase response of the measured impedance tensors. Banks and Wright (1998) proposed a "holistic" approach in determining *regional* geoelectric trends by expanding on the fact that the presence of a regional 2D structure will manifest itself in the common phase of impedance tensor elements belonging to the same column vector. These elements can be regarded to be electric fields produced by a magnetic field parallel or perpendicular to the regional strike. Accordingly, if a group of MT soundings share the same regional response, regardless of the amount of local effects experienced by individual soundings, the real and imaginary parts of the electric fields rotated to the direction of the regional response will plot on a line of constant phase in the complex plane. Conversely, the direction parallel to which we find the best fitting straight line between the real and imaginary parts may be used as a criterion for determining the regional strike. It should be noted that this is a form of

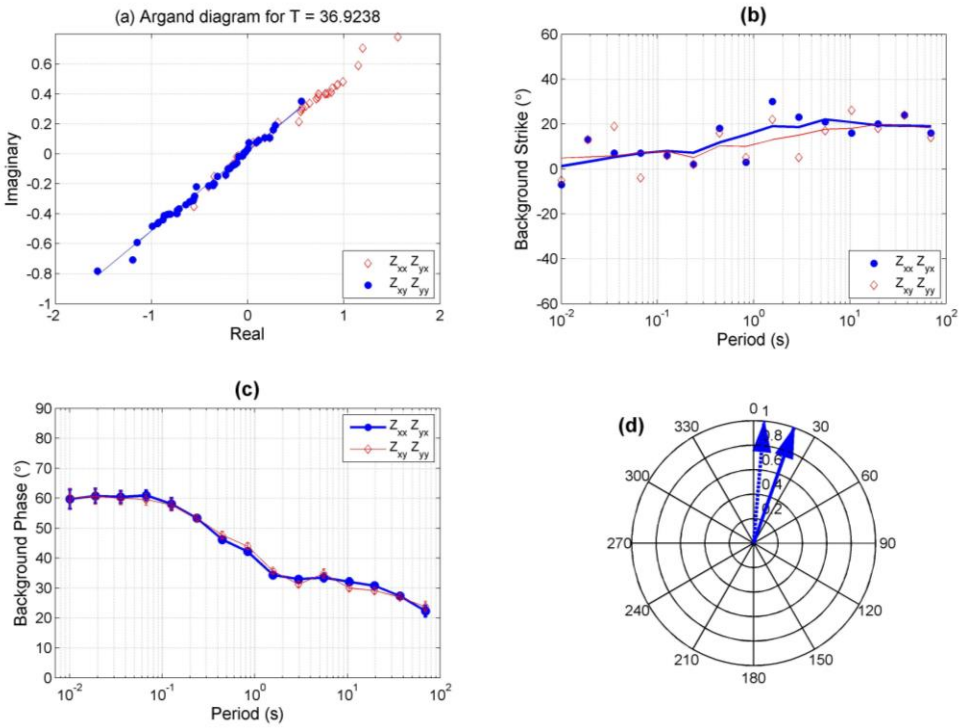

Figure 6.6: Determination of the background geoelectric strike from the MT Tensor Impedance data after Banks and Wright (1998). **(a)** Best fitting of all straight lines fitted to the Argand diagram of the rotated telluric (column) vector $[Z_{xx}(\phi)\ Z_{yx}(\phi)]^T$, for the interval 20-50s it is found at the azimuth of ~N20° (solid blue circles). The open red diamonds are the corresponding elements of the telluric vector $[Z_{xy}(\phi)\ Z_{yy}(\phi)]^T$, the azimuth also being ~N20°. **(b)** The frequency dependent background strike extracted from all MT data. Solid blue circles indicate the strike estimated from $[Z_{xx}(\phi)\ Z_{yx}(\phi)]^T$; open red diamonds correspond to $[Z_{xy}(\phi)\ Z_{yy}(\phi)]^T$; the continuous solid lines are smoothed versions of the corresponding discrete curves. **(c)** The corresponding regional phases. **(d)** Range of variation of the background strike: the dashed arrow indicates the mean background strike at short periods; the solid arrow is the same for long periods.

hypothetical event analysis, whose basic idea is described by Ritter and Banks (1998).

This concept is implemented by rotating the impedance tensor incrementally by an angle $\phi_i = \phi_{i-1} + \Delta\phi$, $\phi \in [-90°,90°]$, and fitting a straight line to the real vs imaginary parts of each column vector $[Z_{xy}(\phi)\ Z_{yy}(\phi)]^T$ and $[Z_{xx}(\phi)\ Z_{yx}(\phi)]^T$ of the impedance tensor. The angle ϕ_0 at which we find the minimum of all misfits should be the direction at which the elements of each column vector have the same phase. For instance, in the frequency interval 20-50s, this best fitting line is found at the strike direction N20° (Fig. 6.6a). The regional phase is the arctangent of the slope. Repetition of the procedure over several consecutive narrow frequency intervals in the measured band of 130Hz-100s, yields the frequency dependent curves of the background strike direction ϕ_0 (Fig. 6.6b), and the corresponding regional phases (Fig. 6.6c).

The background strike is rather unstable if not erratic at short periods, where it exhibits a N-S average orientation, and rather stable at long periods (T > 1s), where it indicates a well-defined N20° orientation consistent with the strike of F1 and F2 systems and the Lakki plain (Fig. 6.6b). By comparison to Fig. 6.5, it is now clear that at the southern part of Lakki the (younger) F4 system is locally dominating EM induction and comprises a major component of hydrothermal activity. It is also interesting to note that the regional phase indicates the existence of two background conductors: one shallow, evident at periods shorter than 0.2s and presumably associated with the hydrothermal field, and one evident at the interval 2s – 30s and presumably associated with a deeper structure of the volcano's interior.

3.3 Two-dimensional inversion

Based on the above discussion, it is possible to conclude that the weak to moderate 3-dimensionality of the observed responses is a consequence of local 3-D induction due to low-contrast geoelectric inhomogeneities, superimposed on a dominantly 2-D background. In such case, the data can still be interpreted with 2-D inversion tools; the local 3-D effects will not be fully resolved, but the more significant part of the conductivity structure, i.e. reservoirs and main fluid circulation zones will still be detectable. However, in order to implement 2-D inversion techniques we need to define the TE/TM modes of induction over the study area.

Although the impedance and magnetic transfer function responses measured at a given period interval do not normally originate at the same depth range, the configuration of the induced electric and magnetic fields is tell-tale of the principal mode of induction in the vicinity of a sounding. Accordingly, the mode of induction can be inferred by studying the configuration of the maximum polarization ellipses and real induction vectors:

a) Inside of the caldera, along the west flank of Lakki between sites 902B – 905B, as well as 902R and 901R, the approximate orthogonality of the polarization ellipses and real induction vectors is consistent with TE mode of induction over a NNW-SSE conductive dyke – the dyke presumably being the F4 fault zone.

b) Inside of the caldera, at the SW flank of Lakki, as well as along the west flank between sites 906B and 119B, the polarization ellipses and induction vectors are similarly oriented and consistent with TM induction above the resistive part of a NNE-SSW oriented lateral conductivity interface.

c) Inside of the caldera and along the east side of Lakki, between sites 908R (Stephanos crater) and 119R, the orientation of the polarization ellipse is, by inference, consistent with TE induction

over a NNE-SSW conductive dyke, which in this case is presumed to be the F2 fault zone.

d) Outside of the caldera, SW of Lakki, the orientation of the polarization ellipse is consistent with TE induction over a NNE-SSW conductive dyke, which again is presumed to be the F2 system. This interpretation is strongly corroborated by a multi-parametric geophysical survey conducted by Lagios and Apostolopoulos (1995) in that area, which has detected circulation along planes of orientation consistent with that of F2.

The two-dimensional inversion has been carried out with the algorithm of Rodi and Mackie (2001), along transects AA΄ and BB΄ of Fig. 6.2. The TE and TM modes were simultaneously inverted, using the spatial configuration described above. A finely discretized homogenous half-space with topography, bathymetry and seawater taken into consideration was used as a starting model; the discretization scheme is apparent in Fig. 6.10 and Fig. 6.11. Several inversions with different starting models and regularization factors were carried out before the final models were declared. The quality of the final models can be summarized as follows:

West Transect (AA′): The observed and residual TM and TE apparent resistivity and phase responses can be studied in Fig. 6.7. It is apparent that the observed responses are rather successfully reproduced and the final χ^2 misfit is 1357 with an expectation value of 952. The higher than expected χ^2 can be attributed to the moderate local 3-D effects observed at some sounding locations, which cannot be adequately modelled with 2-D interpretation tools, as well as to the low uncertainty (observational error) associated with the measurements (e.g. Fig. 6.3 and Fig. 6.4).

East Transect (BB′): The observed and residual TM and TE apparent resistivity and phase responses can be studied in Fig. 6.8. It is apparent that the observed responses are approximated well and the final χ^2 misfit is 1781 with an expectation value of 976. It is rather easy to see that as to the quality of the inversion and the higher than expected χ^2 the same comments as per the West Transect apply.

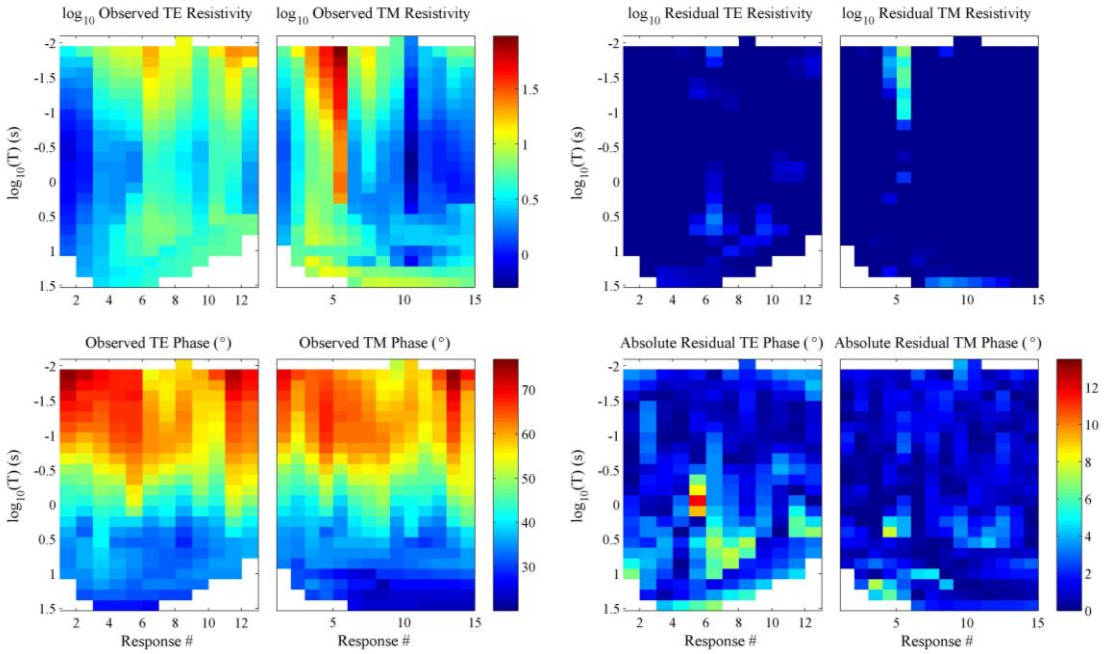

Figure 6.7: Observed (left panels) and residual (right panels) apparent resistivities and phases along the West Transect (AA′ in Fig. 6.2). Each column corresponds to one sounding curve; the order of columns corresponds to the order of soundings along the Transect.

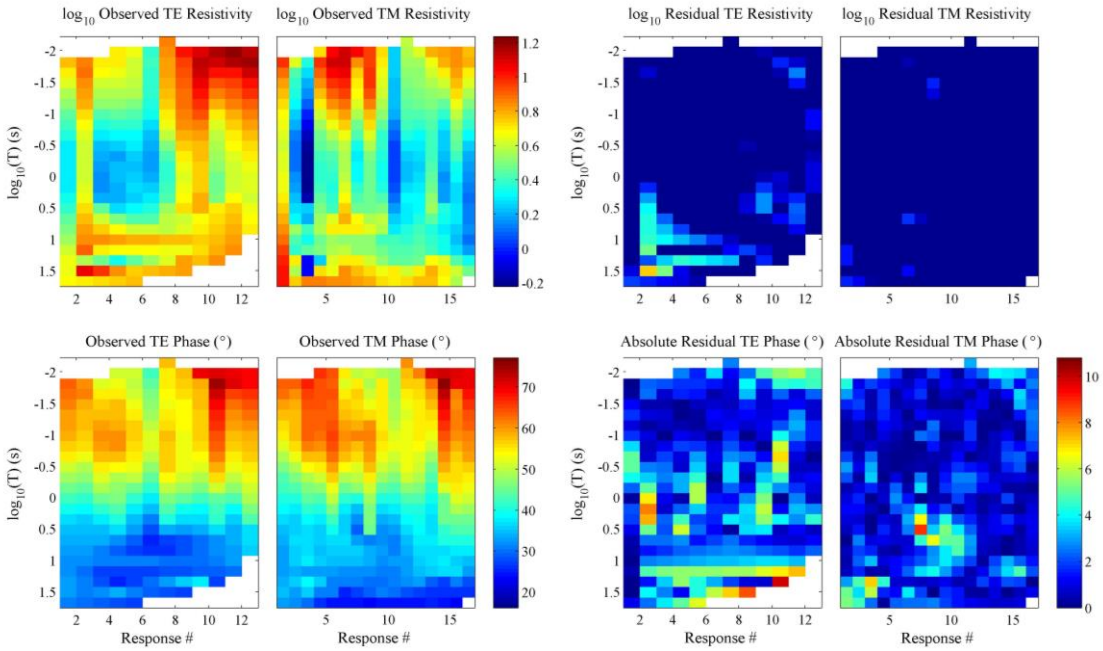

Figure 6.8: Observed (left panels) and residual (right panels) apparent resistivities and phases along the East Transect (BB′ in Fig. 6.2). Each column corresponds to one sounding curve; the order of columns corresponds to the order of soundings along the Transect.

4. The Geoelectric Structure

4.1 Constraints from borehole data.

Fig. 6.9 combines data from the two test wells N1 and N2 (Ungemach, 1983; Geotermica Italiana, 1983), and vertical resistivity profiles extracted from nearest to the boreholes locations of the East and West transects respectively. Available borehole data include: **(a)** The lithological columns. **(b)** Open microfracture domains which, in general correspond to fault zones and exhibit high hydraulic (fracture) permeability, associated with considerable or total loss of drilling fluid. **(c)** Temperature data as determined inside the boreholes. Geophysical well logging was not performed, mainly due to the high temperature and pressure conditions. Hydraulic permeability was determined from the rates of loss of drilling fluid and macroscopically, from fractures observed in recovered rock cuttings. Porosity had to be determined from cuttings. According to the well logs, the caldera infill has undergone extensive argillization, the degree of which reduces with depth. Lava formations experience, in general, less severe alteration than tuff strata. However, some (e.g. brecciated) lavas are more altered and exhibit a high degree of secondary porosity and porous permeability. The tuffs are almost completely devitrified; this process is much more extensive in thick(er) and homogeneous, than in thin(er) and inhomogeneous formations and has generated significant secondary porosity, (or caused manyfold increase if some pre-existed). In the upper 300m (argillic zone), the main product of alteration is the very hydrofile smectite (of the group of montmorillonites).

At depths greater than 300m, phyllic alteration takes place, which generates less hydrofile minerals. Wet clay formations are known to give very high electrical conductivity signatures. Unfortunately we do not have detailed quantitative data about the fractional distribution of clay minerals with depth and cannot

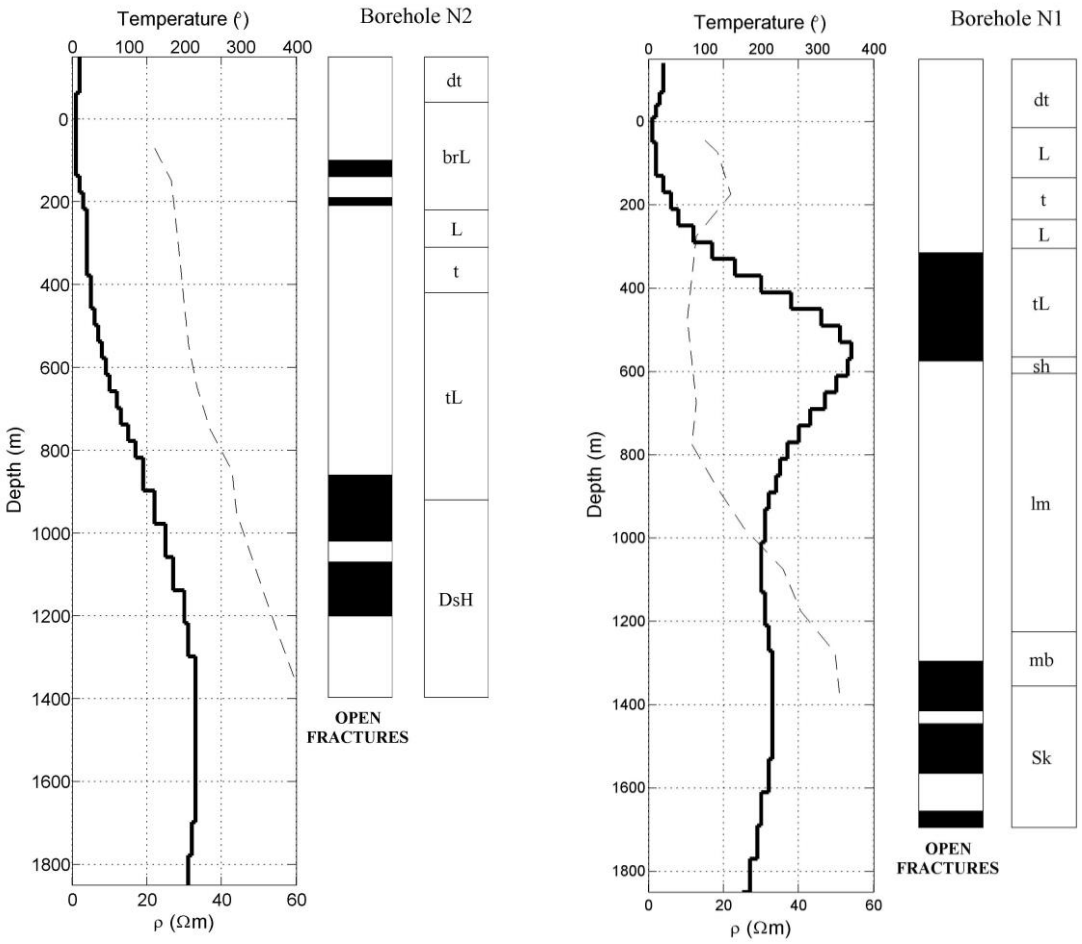

Figure 6.9: Correlation of borehole N2 (left) and borehole N1 (right) with the vertical resistivity profiles extracted from nearest to the boreholes locations of the West (left) and East (right) transects respectively. Borehole information was taken from the technical reports of Ungemach (1983) and Geotermica Italiana (1983). Black shading indicates the domains characterized by open fractures and high hydraulic permeability. Lithological abbreviations are as follows: **dt**, detritus; **brL**, brecciated lava; **L**, lava; **t**, tuff; **tL**, tuff and lava; **DsH**, dioritic subintrusives and hornhels; **sh**, shales; **lm**, limestone; **mb**, marble; **Sk**, skarn.

assess their relative contribution to the observed electrical conductivity. Only qualitative interpretations can be made, although it is certain that at shallow depths, both factors will cooperate to produce very low resistivities. The reduction of the degree of argillization and the transition to the phyllic zone at depths greater than 300m should produce a detectable overall increase of electrical resistivity within the caldera. The borehole data indicate the existence of a hot water reservoir at depths of 150-300m below mean sea level. Stephanos phreatic explosion crater also attests to the presence of an aquifer at these depths, inasmuch as analysis of the crater's geometry places the focus of the explosion (and the feeder aquifer) at depths 160-200m below sea level. N2 indicates a second concentration of geothermal fluids at depths of 900-1300m and N1 finds a similar formation at 1300-1700m.

Correlation of N1 and East Transect: The shallow structure is very conductive, with a 1Ωm conductor appearing at, and just under sea level. In the lithological column, this corresponds to highly altered, low permeability detritus, lava and tuff formations. Given that such depths lie in the argillic alteration zone, it is reasonable to assume that this conductor represents the combination of high fractional volumes of hydrous clay minerals and electrolyte concentration. The temperature exhibits a local peak of approx. 150°C at depths of 160-200m, which coincides with the floor of the argillic-phyllic alteration zone. The

temperature increase corresponds to a shallow hot water reservoir and is associated with an increase in resistivity to approx. 6-8 Ωm, which may be explained in terms of a significant reduction in the fractional volume of hydrous clay minerals within the phyllic alteration zone.

The temperature drops significantly to 70–90°C at depths 300–800m, in coincidence with a fractured, highly permeable domain at depths of 310–600m, which is associated with total loss of drilling fluid and can be attributed to faulting, as it is consistent with the expected positions of fault planes belonging to the F2 system and the gravity fault zone produced by the collapse of the volcano walls during the formation of the caldera. This may imply infiltration of cold seawater spreading to N1 through the F4 and F2 system. Between 600m and 900m N1 penetrates the low-permeability pre-volcanic basement (limestones), which has been thermally metamorphosed to marble below 1250m. At depths greater than 1360m the drill enters the halo of an old, fractured dioritic intrusion (skarn). According to Vougioukalakis (1993) this should not be younger than 24Ka. The temperature exceeds 300°C. There is only partial loss of drilling fluid in the fractured domain, indicating medium to high permeability. The origin of the fracturation zone may be partially blocked fault zones, or the emplacement of the dioritic intrusion, or a combination of both factors. At any rate, a deep fluid circulation zone and reservoir appears to develop at 1350-1700m, within the fracturation zone

At depths greater than 300–400m, the resistivity profile does not correspond to the lithological column at N1 because the former correspond to formations located within the caldera and at the hanging wall(s) of the F2 system, while the latter is outside of the caldera and at the footwall(s). The resistivity increases locally to approx. 54 Ωm at the depth of 600m; this can be explained in terms of a dioritic intrusion, possibly the same as that detected in N1 and very likely the same as the one detected in N2 (see below for details). The resistivity drops to approx. 30 Ωm at depths greater than 900m, remaining at this level to at least 1800m and further decreasing at greater depths. Such values and variation are comparable to those observed near N2 and, together with the data of that borehole, indicate the possibility of a deep circulation zone and reservoir at 1300–1800m depth.

Correlation of N2 and West Transect: The detritus observed in the lithological column is associated with very high permeability up to 50m below sea level and is imaged as a good (approx. 2 Ωm) conductor. The resistivity profile exhibits a very conducting zone of approx. 1Ωm at depths 50–150m below sea level, which in the lithological column is associated with a highly altered chaotic formation comprising fractured tuff breccia and subordinate lavas and scorias in blocks – brecciated lavas or brL in Fig. 6.9. Given that these depths are in the argillic alteration zone, as well as the intense hydrothermal activity of the area, it is reasonable to assume that the conductor represents a combination of electrolyte concentration (shallow reservoir) and clay mineralization.

The depths 100-210m are characterized by the presence of two fracturation zones associated with total loss of drilling fluid, which are situated at the lower parts of the brecciated lavas. The disturbed lithology is likely to be due to the emplacement of the nearby post-caldera rhyo-dacite domes. This is a plausible cause of fracturing, but the fact that fractures are open (total loss) should probably be attributed to concurrent faulting, which we are inclined to associate with the F1 and F3 systems. The well logs do not elucidate this problem but they contain indication that these fractured domains are part of a fluid circulation zone. Notably, a water bearing formation at 150-300m depth has been confirmed by N2; this corresponds to a good 2–4 Ωm conductive domain extending between 150–400m and overlapping with the depth extent of the fracturation zone. According to the well logs, such depths correspond to the phyllic alteration zone. Thus it appears plausible that residual fracturation from the emplacement of the rhyo-dacites and contemporary faulting combine to develop a circulation zone which is likely to feed a

"shallow reservoir" in the argillic alteration zone imaged as a very good 1 Ωm conductor, as well as a circulation zone and deeper reservoir in the phyllic alteration zone imaged as a good 2 – 4 Ωm conductor.

The circulation zone is followed by a gradual increase in resistivity to approx. 35Ωm at 1300m below sea level and a corresponding increase in temperature. It is noteworthy that regardless of the increase, the resistivity still remains at rather low levels! Moreover, the steadily increasing temperature indicates the absence of direct contamination by cold sea water infiltration, as is the case with N1. In the lithological column this range of depths corresponds to a low permeability zone comprising almost completely altered and devitrified tuffs and lavas, (L and t in Fig. 6.9), followed by an intercalation of breccia and andesitic or dacitic lavas, sometimes in blocks (tL in Fig. 6.9). All these formations belong to the phyllic alteration zone; fractures are totally absent, but the material has secondary porosity. In consequence, we interpret the gradual resistivity increase in terms of a corresponding gradual decrease of the concentration of hydrophile clay minerals in the complex background of hydrothermally altered material produced by the formation of the caldera and subsequent emplacement of volcanic intrusives.

The depths 900m-1200m are characterized by intense fracturing and very high permeability. Between 1200-1400m, where N2 was terminated, fracturing cannot be observed albeit permeability is still appreciable. The fractured zone can be interpreted in terms of faulting although it is difficult to pinpoint the responsible fault(s). The lithology of the fractured domain consists of a sequence of quartz dioritic intrusives and intercalated calcsilicate and quartz feldspathic hornferls comprising the halo of a dioritic intrusion, which may be related to the one observed at N1. The MT data do not detect an impressive conductor at 900-1200m, but it is noteworthy that the rate of resistivity increase slows significantly after approx. 1100m and becomes negative after approx. 1700m. This behaviour is consistent with the existence of a deep circulation zone and reservoir, as suggested by previous interpretations of the borehole data (e.g. Ungemach, 1983; Geotermica Italiana, 1983).

4.2 West Transect (AA')

Fig. 6.10 illustrates the (logarithm) of the resistivity structure as reconstructed by 2-D inversion. At the SW extension of the Lakki graben, outside of the caldera, the structure exhibits a shallow (less than 0.25km) and a deep (0.75–2.5km) conductive zone. It also appears that the latter is connected with the caldera through a relative conductor seen at depths 0.5–0.8km and distances 1–1.5km along the profile. We are inclined to interpret these geoelectric features as epiphenomenal to fluid circulation in the F1/F2 system.

The gravity fault comprising the southern boundary of the caldera is rather clearly resolved. At depths shallower than 1 km it is outlined by an interface between a relative resistor to the south (foot wall) and a relative conductor to the north (hanging wall), located between 1.4 and 1.6 km along the transect, as indicated in Fig. 6.10. At depths greater than 1 km, it can be seen as a lateral discontinuity (notch) in a relatively resistive formation, located between 1.5 and 2 km along the Transect. The northern boundary is not directly observable; its position is postulated by a long-dash line extrapolated from the surface.

The resistive formation observed at depths between 0.8 and 2.5km beneath the Caldera is almost ideally situated, so as to be identified with the dioritic intrusives found by drilling at N2 (the ceiling of the intrusion is pointed to with an arrow). The floor of the caldera cannot be clearly identified; its location depends on the age of the intrusion which, as mentioned above, is older than 24Ka. Thus, if it is pre-calderic, the floor should be sought near the ceiling of the intrusion, approximately as indicated by the dotted line. If it is syn- or post-calderic, then it is apparently lying deeper, perhaps as deep as 2km (dashed line).

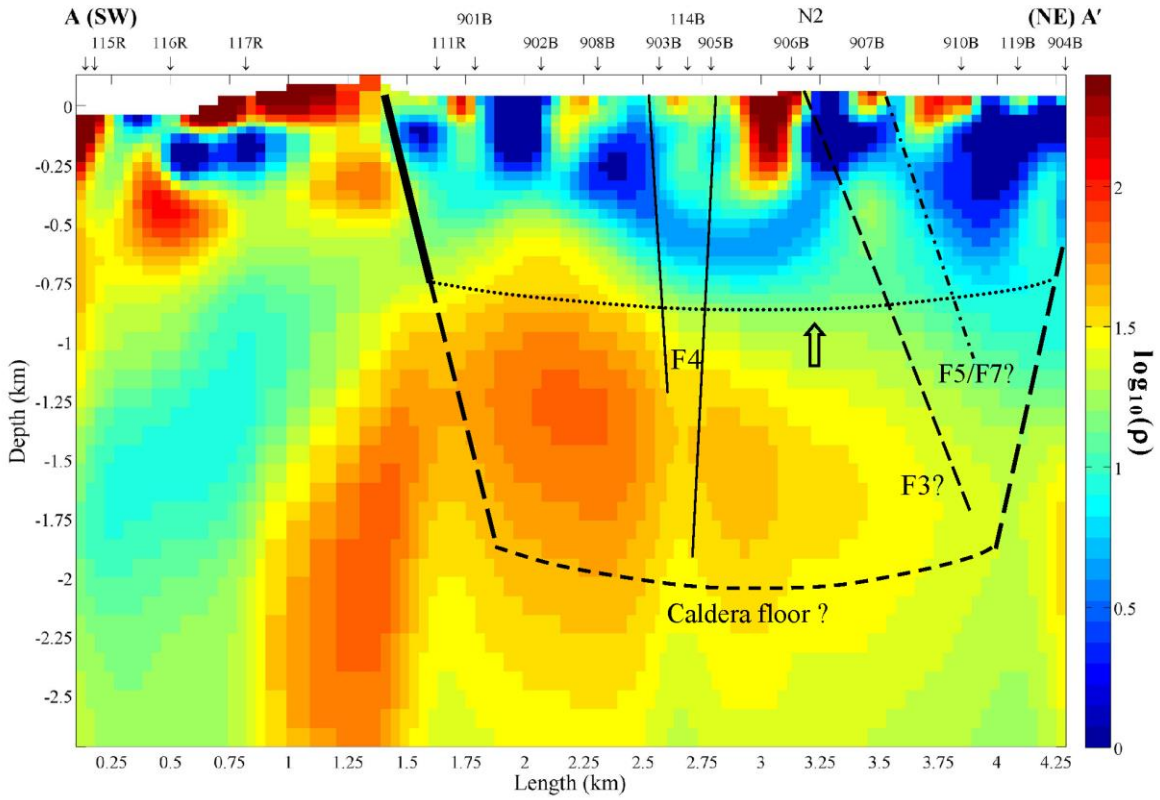

Figure 6.10: Two-dimensional best-fitting model of the resistivity structure along the West Transect A-A′. N2 marks the nearest to N2 location of the Transect. The arrow points to the ceiling of the dioritic intrusion at N2.

The horizontal dotted line indicates the approximate depth extent of the geothermal system which, evidently, comprises an interconnected network of reservoirs and circulation zones. According to the discussion above, good conductors up to 0.25km deep represent the combined effect of clay mineralization and fluid concentration in the argillic hydrothermal zone. Deeper (0.25 – 0.8km) conductors more likely represent fluid concentration and circulation in the phyllic hydrothermal zone. The deep circulation zone detected in relation to the deep permeable zone at N2 belongs to this part of the system.

As noted above, the deep circulation zones are associated with contemporary faulting. The solid lines marked F4 connect the projected intersections of F4 with the Transect at the surface, through a deep lateral resistivity discontinuity (notch) in the dioritic intrusion, to a rather good conductor at depths greater than 2km. The plunge of the lines is consistent with the apparent dip of the F4 faults at their intersection with the Transect. Given the significance of F4 in the function of the hydrothermal system, we interpret the low resistivity notch to be an epiphenomenal signature of the permeable fault zone through which hydrothermal fluids convect.

The bell shaped dome located between sites 906B and 910B and peaking at approx. 0.28km beneath site 907B is interpreted to be part of the dioritic intrusion. It is noteworthy that the resistivity of the dome decreases from approx. 20Ωm at the depth of 0.45km to approx. 12Ωm at depths 0.6 – 0.75ckm. The long-dash line marked F3 starts at the approximate position of the intersection of F3 with the Transect at the surface and plunges at an angle of 70° to the NE; it can easily be seen to pass through the zone of decreased resistivity, which can thus be interpreted as an epiphenomenon of faulting (fluid circulation). The downward extrapolation of same line connects with yet another low-contrast lateral discontinuity in the deeper resistivity structure, located at depths 1.5 – 2.5 km at a distance of approx. 4km along the

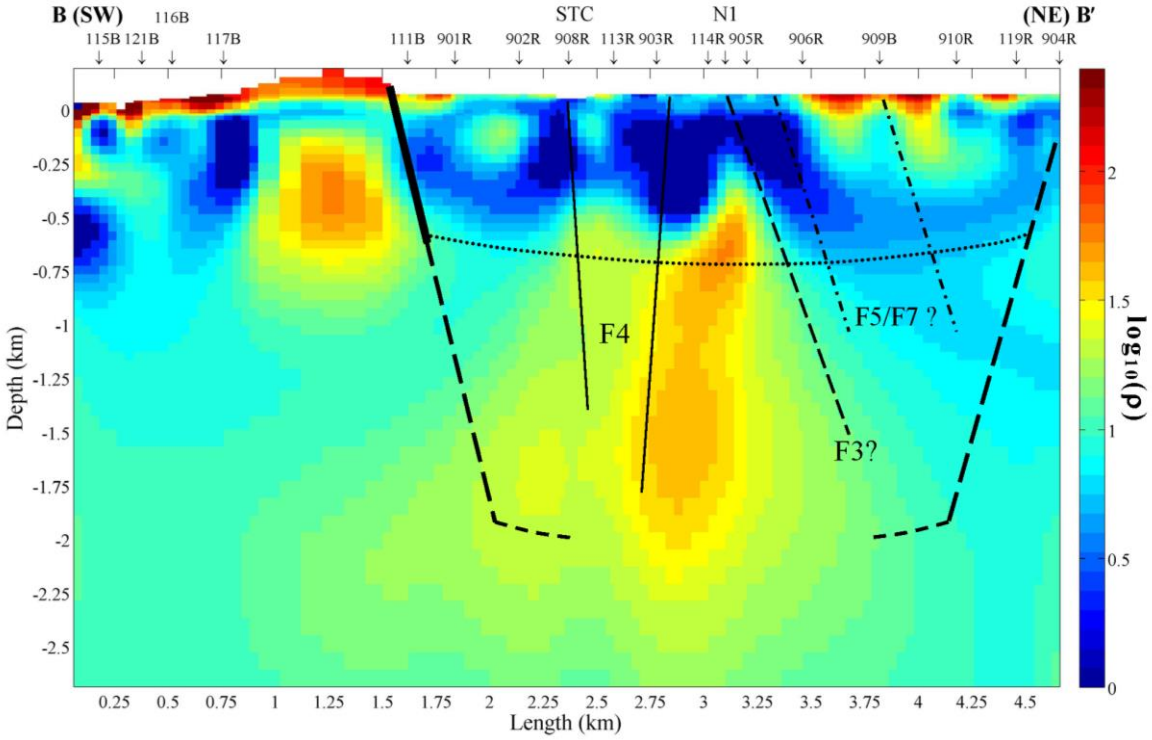

Figure 6.11: Two-dimensional best-fitting model of the resistivity structure along the East Transect B-B′. STC marks the position of Stephanos phreatic explosion crater; N1 marks the nearest to N1 location of the Transect.

Transect. This is also interpreted to result from the combined effect of several converging faults.

Northward of site 907B, the shallow and deep circulation zones appear to be controlled by the fault network. In addition to F1, F2 and F3, possible "culprits" are the faults of the F5 secondary system. Just to give an example, the dash-dot line marked F5/F7 starts at the projected intersection of a significant F5 and F7 fault with the Transect and plunges at 70° to the NE; this may adequately explain a significant part of the resistivity structure observed in the vicinity of the West Transect.

4.3 East Transect

Fig. 6.11 illustrates the logarithm of the resistivity structure, as reconstructed by the 2-D inversion. At the SW extension of the Lakki depression (outside of the caldera), the structure is generally more conductive in comparison to the corresponding stretch of the West Transect, although the two profiles are separated by only a few hundreds of meters: the shallow and deep conductive zones detected in the West Transect appear to have merged and their connection to interior of the caldera has become, both at sea level and at depth. We are inclined to attribute the significant change (decrease) in resistivity to fluid circulation and diffusion associated with the F2 system of faults.

The gravity fault defining the southern boundary of the caldera is observable at depths shallower than 0.8km as an interface between a relative resistor to the south (foot wall) and a good conductor to the north (hanging wall), located between 1.5 and 1.7 km along the Transect. Fumaroles exist on the south wall of Lakki and in the vicinity of F2 (see Fig. 6.1); therefore, the good conductor associated with the hanging wall defines the extent of the circulation zone feeding the fumaroles. At depths greater than 1 km an interface cannot be seen and the boundary is drawn by extrapolation. The northern boundary is not observable and is indicated by a long-dash line extrapolated from the surface. The steeply dipping

conductor between sites 119R and 904R may be related to circulation along the associated gravity fault.

The relatively resistive formation observed at depths between 0.4km and 2.3km is attributed to the same dioritic intrusion as that observed in the West Transect and found by drilling at N2. In consequence and as per the West Transect, the location of the floor depends on the age of the intrusion: it is either located in the vicinity of the horizontal dotted line, or at depths of the order of 2km (dashed line).

The horizontal dotted line again indicates the approximate depth extent of the hydrothermal system. We reiterate that according to the analysis of the borehole data, the shallow, very good conductors located at depths up to 0.25km represent the combined effect of clay mineralization and fluid concentration in the argillic hydrothermal zone, while the deeper (0.25–0.5km) good conductors more likely represent fluid concentration in the phyllic hydrothermal zone.

As also repeatedly noted above, the deep circulation zones are associated with contemporary faulting. Inside as well as outside of the caldera, the geoelectric structure is more conductive in comparison to the corresponding stretch of the West Transect, although the two profiles are separated by a few hundreds of meters. Noting, however, that inside the caldera, the East Transect runs literally on top of the main F2 fault, it is reasonable to propose that the overall lower resistivity is a consequence of increased fluid circulation and diffusion in the immediate vicinity of F2, particularly at the southern part of Lakki.

The lines marked F4 connect the intersections of F4 with the East Transect at the surface, through a very good sub-vertical conductor extending between 0.05 – 0.4 km directly beneath site 908R, to a low resistivity notch in the postulated dioritic intrusion and to a rather good conductor at depths greater than 2km. The shallow conductor lies directly beneath Stephanos and is thought to represent the combined effect of clay mineralization and fluid circulation through F4. The plunge of the lines is consistent with the apparent dip of the faults at their intersection with the Transect so that the low resistivity notch is again interpreted as the signature of the fault zone through which hydrothermal fluids convect.

The line marked F3 starts at the projected intersection of the Transect with trace of F3 at the surface, and plunging at approx. 70° to the NE, through a similarly dipping very good conductor, defines the boundary of the inferred dioritic intrusion. The geoelectric structure of the hanging wall of F3 appears to be very conductive. As in the West Transect, the shallow and deep circulation zones northward of site 905R may be augmented by faults additional to F2 and F3, specifically those of the F5 and F7 secondary system. As an example, the dash-dot lines marked F5/F7 start at the projected intersections of F5 and F7 faults with the Transect and plunge at 70° to the NE: it is apparent that they may explain several details related to the distribution of near-surface conductors in the vicinity of the Transect.

5. Discussion and conclusions

In this study, we present an updated analysis a 39 single-site Magnetotelluric soundings conducted in the late 80's and early 90's in Nisyros, a small island volcano at the eastern end to the Hellenic Volcanic Arc (Greece). More precisely, the survey was carried out in the Lakki graben, a small elongate basin formed by a system of NNE-SSW antithetic normal faults running across the island and through the eastern half of Nisyros caldera, which contains a hydrothermal field and high temperature geothermal resource.

The "update" included re-processing of the raw data with a robust Earth response function estimation method, the application of advanced hypothetical event analysis techniques to study the spatial properties of the telluric field, separate induction modes and prepare the data for quantitative interpretation with two-dimensional inversion. In a final step, 2-D inversion was carried out along two parallel profiles arranged in the longitudinal direction of the Lakki graben. This exercise yielded satisfactory fitting

between observed and calculated responses and rather well-constrained reconstructions of the resistivity structure, including detailed electrical images of fluid reservoirs, circulation and diffusion zones and hydrothermal convection paths.

The geoelectric structure is shown to comprise a quasi-two-dimensional, low-contrast background defined by the regional (first order) faulting systems and decorated by local, low-contrast three-dimensional resistivity inhomogeneities. Low resistivity contrasts are the reasons why in spite of local three-dimensionality, 2-D inversion could successfully reconstruct the principal elements of the geoelectric structure. The low contrasts may be the outcome of continuous intense tectonic and hydrothermal activity resulting in extensive lateral fluid diffusion and pervasive alteration that smears any original high resistivity contrasts, even in a domain as structurally inhomogeneous, as a volcanic caldera. The effects of such processes are much more prominent at shallow depths (up to 1km), where it is easier for fluids to diffuse (also facilitated by higher effective porosities and lower lithostatic pressures). This is also the reason why the reconstruction (fitting) was more successful at the short-period half of the measured bandwidth.

The resistivity structure at depths 100-300m is characterized by a number of interconnected, very low resistivity enclosures (<2Ωm) which are thought to correspond to fluid concentrations (reservoirs) within the argillic alteration zone. At depths between 300m and 1km, these merge into laterally extended low resistivity (<12Ωm) zones which are thought to represent fluid concentrations and circulation in the phyllic and phyllic-propylitic alteration zones (hence the increased resistivity). Unfortunately, the absence of precise data on the fractional volume of clay minerals does not allow a reasonable estimation of the liquid fraction and storage capacity. The development of reservoirs and the lateral circulation and diffusion of fluids at all depths may have been facilitated by both major and minor fault zones, often resulting in the formation of fault-aligned epiphenomenal conductors. At the southern half of Lakki, where the hydrothermal field is located, the caldera boundary faults and systems F1, F2 and F4 appear to be major contributors. At the northern half of Lakki, F2, F3, F5 and F7 appear to have more prominent effect.

The deep (>1km) and more important convection and circulation zones are generally associated with major faults and their intersection. Compelling evidence is presented, indicating that the most significant of those are a system of NE-SW oriented active normal faults (identified as F1 and F2 in Fig. 6.1), intersecting with a conjugate system of NNW-SSE normal faults identified as F4, which is particularly active at the SW sector of the island and defines the main convection path. One line of such evidence relates to the configuration of telluric current flow in the area of most intense thermal activity, at the southern part of Lakki, which has a definite NNW-SSE orientation and correlates with the orientation of F4, as well as with the alignment of thermal phenomena (fumarolic activity, phreatic explosion craters and debris flow and lacustrine deposits related to phreatic explosion events). It is almost straightforward to define a causal connection between active normal faulting and telluric current flow because the conductivity of near surface rock formations is principally electrolytic and depends on the salinity of the liquid fraction, the temperature and the presence (or absence) of clay minerals which may increase the salinity by orders of magnitude through ion exchange interactions and/or hydrolysis. Whereas convection/ circulation conduits identify with active normal fault zones, it becomes apparent that electric current should flow easier parallel to the fluid-filled conduits than across them.

At depths between 1km and 2km, the fault-aligned fluid convection paths associated with F4 have been

imaged as sub-vertical low-resistivity zones etched on relatively more resistive background (presumed dioritic intrusion), which connect the shallow conductive structure with deep conductors presumably related to the heat source. Analogous images have been obtained for the caldera boundaries, which are more or less clearly outlined.

Due to the overall low resistivity of the structure, the long periods of the measured Magnetotelluric field could not penetrate to depths greater than approx. 3km. In consequence, the heat source in the form of a magma chamber, such as the one inferred to exist at depths of the order of 7km (Lagios et al., 2005), was not detected: only the conductive halo of the heat source could be probed.

Overall, our analysis has provided detailed images of the volcano's interior, useful information on its geothermal potential and valuable insight into its structure and function. It should be emphasized, however, that the results and conclusions are still approximate: local 3-D induction effects, albeit weak, could not be fully resolved and their effect on the details of the resistivity structure cannot be assessed. It is also difficult to assess the true variation of resistivity between the parallel 2-D transects, which is very important in understanding the geothermal system from both the academic and practical points of view. Such problems can be addressed with 3-D inversion which is expected to provide definitive images of the geoelectric structure and convection paths. This is a challenge to be taken up and reported in the immediate future.

References

Bachmann O, Deering, CD, Ruprecht JS, Huber C, Skopelitis A, Schnyder C (2011) Evolution of silicic magmas in the Kos-Nisyros volcanic center, Greece: a petrological cycle associated with caldera collapse. Contrib. Mineral Petrol. doi:10.1007/s00410-011-0663-y.

Banks RJ, Wright D (1998) Telluric analysis of distributed magnetotelluric impedance measurements, Annales Geophys Suppl. (1-16), C275. In XXIII EGS Gen. Assembly, Nice, France, 20-24 April 1998.

Bohla M, Keller J (1987) Petrology of plinian eruptions of Nisyros volcano, Hellenic arc. Terra Cognita, 7: 171.

Davis E (1967) Zur Geologie und Petrologie der Inseln Nisyros und Jali (Dodekanes). Praktika Academy of Athens 42: 235-252.

Dawes GJK (1984) Short Period Automatic Magnetotelluric (S.P.A.M.) system. In: A Broadband Tensorial Magnetotelluric Study in the Travale-Radicondoli Geothermal Field. In: EC Final Report, Contract No. EG-A2-031-UK.

Dawes GJK, Lagios E (1991) A Magnetotelluric Survey of the Nissyros Geothermal Field (Greece). Geothermics 20(4):225–235

Di Paola GM (1974) Volcanology and petrology of Nisyros island (Dodecanese, Greece). Bull Volcanol 38:944-987.

Egbert GD, Booker JR (1986) Robust estimation of geomagnetic transfer function data. Geophys J R astr Soc 87:173-194.

Francalanci L, Vougioukalakis GE, Perini G, Manetti P (2005) A West-East Traverse along the magmatism of the south Aegean volcanic arc in the light of volcanological, chemical and isotope data: In M Fytikas, G Vougioukalakis *(eds), The South Aegean Volcanic Arc, Present Knowledge and future perspectives*, Elsevier, pp 65-111.

Geotermica Italiana (1983) Nisyros-1 geothermal well. PPC-EEC Report, p 106.

Huber P J (1981) Robust Statistics. Hoboken, NJ, John Wiley & Sons, Inc.

Keller J (1982) Mediterranean Island Arcs. In: Thrope RS (ed) Andesites, Wiley, New York, pp 307-325.

Lagios E (1991) Magnetotelluric study of the Nisyros Geothermal Field. Bull Geol Soc Greece 25(3):393-407.

Lagios E, Apostolopoulos G (1995) Integrated geophysical study of the geothermal system in the southern part of Nisyros Island, Greece. J Appl Geophys 34:55-61.

Lagios E, Tzanis A, Dawes GJK (1991) Audio-Magnetotelluric Survey of Nisyros Geothermal Field, phase II; Report submitted to PPC, Department of Alternative Energy Resources, Athens, Greece.

Lagios E, Sakkas V, Parcharidis I, Dietrich V (2005) Ground deformation of Nisyros Volcano (Greece) for the period 1995–2002: results from DInSAR and DGPS observations. Bull Volcanol 68(2):201–214.

LaTorraca G, Madden T, Korringa J (1986) An analysis of the magnetotelluric impedance tensor for three-dimensional structures. Geophysics 51:1819–1829.

Limburg EM, Varekamp JC (1991) Young Pumice deposits on Nisyros, Greece. Bull Volcanol 54(1):68-77.

Nomikou P, Papanikolaou D (2011) Extension of active fault zones on Nisyros volcano across the Yali-Nisyros Channel based on onshore and offshore data. Mar Geophys Res 32:181-192.

Papadopoulos GA, Sachpazi M, Panopoulou G, Stavrakakis G (1998) The volcanoseismic crisis of 1996–1997 in Nisyros, SE Aegean Sea, Greece. Terra Nova 10:151–154.

Papanikolaou D, Nomikou P (2001) Tectonic structure and volcanic centres at the Eastern edge of the Aegean volcanic arc around Nisyros Island. Bull Geol Soc Greece 34(1):290-296.

Papanikolaou D, Lekkas E, Sakelariou D (1991) The Geological structure and evolution of Nisyros island. Bull Geol Soc Greece 25(1):405-419.

Ritter P, Banks RJ (1998) Separation of local and regional information in distorted GDS response functions by hypothetical event analysis. Geophys J Int 135: 923-942.

Rodi W, Mackie RL (2001) Nonlinear conjugate gradients algorithm for 2-D magnetotelluric inversion. Geophysics 66(1):174–187.

Sachpazi M, Kontoes Ch, Voulgaris N, Laigle G, Vougioukalakis G, Sikioti O, Stavrakakis G, Baskoutas J, Kalogeras J, Lepine Cl, (2002) Seismological and SAR signature of unrest at Nisyros caldera, Greece. J Volcanol Geotherm Res 116:19-33.

Seymour KST, Vlassopoulos D (1989) The potential for future explosive volcanism associated with dome growth at Nisyros, Aegean volcanic arc, Greece. J Volcanol Geotherm Res 37:351-364

Seymour KST, Vlassopoulos D (1992) Magma mixing at Nisyros volcano, as inferred from incompatible trace-element systematics. J Volcanol Geotherm Res 50:273-299.

Sims WS, Bostick FX, Jr, Smith HW (1971) The estimation of magnetotelluric impedance tensor elements from measured data. Geophysics 36:938-942.

Tzanis A (2014) The Characteristic States of the Magnetotelluric Impedance Tensor: Construction, analytic properties and utility in the analysis of general Earth conductivity distributions. arXiv:1404.1478 [physics.geo-ph]. Accessed, 1 May 2017.

Ungemach P (1983) Nissyros Geothermal Wildcut Drilling, Testing, Sampling, 6 June 3 December 1982. Exec. Summary, Preliminary report, EEC Contract No EG-A-1-046-G and EG-A-Y-113-I.

Vanderkluysen L, Volentik A, Hernandez J, Hunziker JC, Bussy F, Principe C (2006a) The petrology and geochemistry of lavas and tephras of Nisyros volcano, Greece. In: Hunziker JC, Marini L (eds) The geology, geochemistry and evolution of Nisyros Volcano (Greece). Implications for the volcanic hazards (44) Mémoires de Géologie Lausanne, pp 79-99.

Vanderkluysen L, Volentik A, Principe C, Hunziker JC, Hernandez J (2006b) Nisyros volcanic evolution: the growth of a stratovolcano. In: Hunziker JC, Marini L (eds) The geology, geochemistry and evolution of Nisyros Volcano (Greece). Implications for the volcanic hazards (44) Mémoires de Géologie Lausanne, pp 100–106

Varekamp JC (1992) Some remarks on volcanic vent evolution during plinian eruptions. J Volcanol Geotherm Res 54:309-318.

Volentik A, Vanderkluysen L, Principe C, Hunziker JC (2006) Stratigraphy of Nisyros vollcano (Greece). In: Hunziker JC, Marini L (eds) The geology, geochemistry and evolution of Nisyros (.

Vougioukalakis G (1989) Geological map of Nisyros Island, 1:25.000, IGME, Athens, Greece.

Vougioukalakis G (1993) Volcanic stratigraphy and the evolution of Nisyros Island. Bull. Geol. Soc. Greece 28(2):239-258.

Wyers PG, Barton M (1989) Polybaric evolution of calc-alkaline magmas from Nisyros, Southeastern Hellenic Arc, Greece. J. Petrol 30:1-37.

Yee E, Paulson KV (1987) The canonical decomposition and its relationship to other forms of magnetotelluric impedance tensor analysis. J Geophys 61:173–189.